Short Communication

Multi-material laser powder bed fusion additive manufacturing of concentrated wound stator teeth

Marcus Oel [a],[*],[1], Johannes Rossmann [b],[1], Behrend Bode [a], Ina Meyer [a], Tobias Ehlers [a], Christoph M. Hackl [b], Roland Lachmayer [a]

[a] *Institute of Product Development (IPeG), Gottfried Wilhelm Leibniz University Hannover, An der Universität 1, Garbsen, 30823, Germany*
[b] *Laboratory of Mechatronic and Renewable Energy Systems (LMRES), HM Munich University of Applied Sciences, Lothstraße 64, Munich, 80335, Germany*

A R T I C L E   I N F O

A B S T R A C T

Additive manufacturing using Powder Bed Fusion by Laser Beam (PBF-LB) enables products with high design freedom. In addition, the ability to process more than one material in all three spatial directions makes it possible to produce highly functional components in one single process. This article investigates whether multi-material manufacturing using PBF-LB is suitable for producing coils for electric motors, which are designed with integrated cooling channels to increase the power density. For this purpose, the copper alloy CuCr1Zr for the coils and the stainless steel 1.4404 (316L) for the core are processed simultaneously. The component designs were verified using 2D and 3D finite element analysis and then manufactured in a multi-material PBF-LB process. While good electrical conductivity of the copper alloy was achieved by heat treatment, it was found that thermal distortion caused deviations from the nominal geometry. The measurement of the electrical properties showed that this distortion leads to short-circuit currents within the coils and the teeth. On this basis, ideas for solutions were developed, with the help of which the functionality of the coils can be ensured or the power density can also be increased. In addition to adapting the design of the component, this includes processing additional or other materials, such as soft magnetic composites.

1. Introduction

Due to the need of a climate neutral transportation, the electrification of the mobility sector is necessary. The field of electric aviation contains a high potential for saving emissions, but due to technical limitations most aircrafts are powered by fossil fuels. As stated in [1], the ratio of power to weight is critical for future electric aircrafts and needs to be increased to make electric aviation possible [2]. Since conventional electric drives do not meet these requirements and are too heavy, other approaches must be explored in order to achieve a high power density to cope with the thermal stress and to avoid overheating [3].

One solution is to optimize the component design to the prevailing thermal loads and requirements. Since conventional manufacturing methods have significant limitations concerning the feasible component shape, other manufacturing processes, such as Additive Manufacturing (AM), must be investigated. AM offers a high degree of freedom with a wide range of different processes. In particular, the Powder Bed Fusion by Laser Beam (PBF-LB) process offers a wide range of applications due to its high accuracy and the large variety of possible materials [4]. In addition to shape and topology optimization, functions and effects can be integrated directly into components [5]. For example, channels can be integrated that are used for lubrication [6], sensor elements can be placed inside components [7], or the structural dynamic behavior can be improved through particle damping [8].

With regard to electric drives, the use of AM has already been investigated with different objectives.

In [9,10], a ceramic isolated copper coil is printed for a switched reluctance machine. Thermal simulations and measurements are conducted, which predict better thermal behavior compared to common windings. In [11], a casted and also a one-component printed coil design made of an aluminium alloy are presented. It is shown, that printed designs in combination with direct liquid cooling enable optimized current densities up to $130\,A/mm^2$, if pure copper is used. A complete multi-material (MM) printed switched reluctance machine is presented in [12], which is made of an iron material, copper and ceramic isolated coils. Results show that the iron losses are, dependent on the electric frequency, up to 100 times higher compared to a laminated core and also worse than soft magnetic composites. In [13], pure copper was printed and compared regarding to mechanical and electrical properties depending on process parameters. Also hollow copper coils are presented. Simpson et al. demonstrate a design method to optimize the coil shape regarding to slot leakage fluxes and current displacement to minimize the AC resistance [14]. The designed coils are also printed with one component. Another coil design for hollow direct liquid cooled coils is shown in [15]. The coils are printed using PBF-LB with copper and aluminium alloy. The used materials are investigated regarding mechanical and electrical properties. In [16], a single phase transformer core is printed consisting of three parts, which are slit into each other. Each part consists of segregated layers to minimize eddy current losses.

It becomes clear that both MM AM and PBF-LB were investigated but not combined.

However, due to recent advances in PBF-LB equipment technology, it is now possible to process different materials in one component [17]. Powder Bed Fusion by Laser Beam using Multi-materials (PBF-LB/MM) expands the degrees of freedom of AM by another dimension and enables the ideal adaptation of the shape to application-specific requirements, but also offers the possibility of locally using the material with the ideal material parameters for the intended application [5].

For the manufacturing in a PBF-LB/MM process a 3D selective MM deposition of the powder is required, where the material also differs within a layer. Therefore an adaptation of the application mechanism of the PBF-LB/MM machine is necessary. The conventional deposition, in which a single blade or brush is used to distribute the powder over the substrate plate, is not suitable for 3D MM applications. Different concepts were compared by Schneck [18] and Mussatto [17]. They are based on vibrating nozzles [19–21], a suction operation between different material coatings [18,22], the use of multiple powder hoppers [23,24], pressurized patterning drums [25] and an electrophotographic powder deposition [26,27]. The manufacturing readiness level of those differs in a range from 2 to 5 [18]. The different coating concepts have different advantages, but there is no concept without disadvantages [17].

Compared to conventional AM, MM deposition has limitations. Besides special requirements for the powder used or a smaller available build space, the biggest disadvantage is the significantly slower coating speed [17]. This is due to the more complex and in some cases multi-step procedure of the coating process. With regard to the materials processed so far in 3D PBF-LB/MM, it is apparent that mainly steel materials and copper or copper alloys have been processed to date, but also ceramics in some cases [18]. The development of process parameters and scanning strategies is significantly more complex with an additional material, although significant improvements can be achieved through the use of artificial intelligence [28]. Research in the field of PBF-LB/MM is currently focused mainly on material science, while there are very few publications on the manufacturing of functional products by the application of PBF-LB/MM. The manufacturing and analysis of an injection nozzle made of tool steel and the copper alloy CW106C [29] and the manufacturing and analysis of thermocouples [30] are to be mentioned in this context.

The aim of this article is to combine PBF-LB and MM AM in the field of electric drives in order to investigate whether PBF-LB/MM is suitable
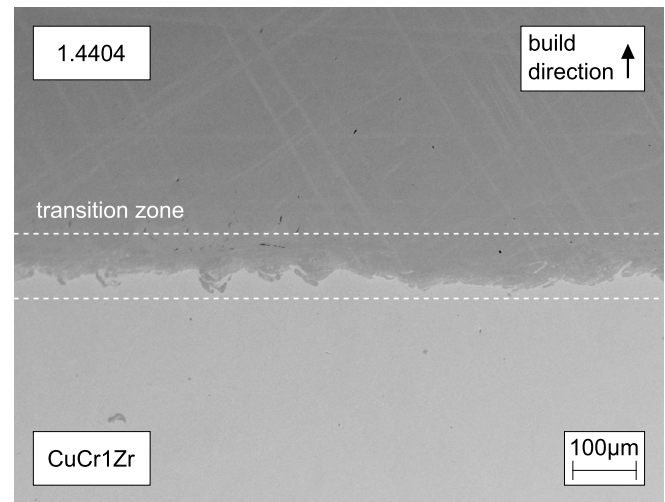

Fig. 1. SEM image of the transition zone between CuCr1Zr and 1.4404.

for the manufacturing of electromagnetic coils for use in electric drives and if an increase in power density can be achieved through the integration of cooling channels. For this purpose, individual teeth are designed with the aid of 2D- and 3D-simulations and manufactured taking into account the process restrictions, and then examined with regard to their geometrical and electrical properties.

2. Theory calculations

Different aspects have to be taken into account to design the required components. Besides electromagnetic requirements, also geometric limitations have to be considered to ensure that the design can be manufactured in the PBF-LB/MM process. Therefore, this chapter shows how the design process is carried out and which constraints are taken into account.

2.1. Geometric limitations

For the PBF-LB/MM process with the system used here, which is described in more detail in Chapter 3.2, there are restrictions of a geometric nature for manufacturing. For example, the build space in the x- and y-directions is limited to dimensions of $240 \times 100\,mm^2$ due to the coating process using drums. Due to the fact that this build area is not supported by the inner wall of the build cylinder, this build area is minimized with increasing component height. A surrounding box is used to ensure a flat powder bed in the area of the printed component and due to the long process time component sizes with a height of up to 30 mm have been carried out. In addition to the maximum component and build area size, the minimum size of individual features or the resolution is also limited. The resolution of the optical system for fusing the powder is mainly determined by the focus diameter of $d_s = 80$ μm. In contrast, the maximum resolution for powder application is a voxel size of 500 μm, which accordingly determines the minimum feature size in the area of a MM transition. In preliminary studies, the mixing of the two materials was investigated using scanning electron microscope (SEM). A SEM image of a material transition zone of a test specimen is shown in Fig. 1. It can be seen that the transition zone has a width of less than 100 μm. Accordingly, it can be assumed that for a gap width of 0.5 mm between areas consisting of 1.4404 or CuCr1Zr, there is no mixing of the two materials.

2.2. 2D electromagnetic motor design

A permanent magnet excited synchronous machine (PMSM) is used as test object. The motor will be designed for a low voltage applica-

Table 1

Initial design data of the PMSM.

Parameter	Symbol	Value	Unit
Slots	Q_s	24	
Polepairs	n_p	11	
Stator outer radius	$r_{s,o}$	66.5	mm
Max. total length	l_{max}	30	mm
Iron length	l_{Fe}	10	mm
Magnet height	h_m	2.3	mm
Rated current density	$J_{s,R}$	6	A/mm^2
Turns per coil	n_c	5	-

Table 2

Materials used in FEA.

Part	Material
Stator laminations	M530-65A
Rotor laminations	M530-65A
Magnets	BMN-48SH
Coils	CuCr1Zr

Table 3

Main data of the PMSM.

Parameter	Symbol	Value	Unit
Rated voltage	$U_{s,R}$	12	V$_{eff}$
Rated current	$I_{s,R}$	47	A$_{eff}$
Rated power factor	$\cos(\phi)$	0.84	-
Rated mech. torque	$m_{m,R}$	3.13	Nm
Rated mech. speed	$n_{m,R}$	2000	rpm
Rated mech. power	$p_{m,R}$	655	W

Fig. 2. Absolute magnetic flux density $|B|$ of one quarter of the motor model excluding cooling channels at $i_s^q = 66$ A.

Fig. 3. Absolute magnetic flux density $|B|$ of one quarter of the motor model including cooling channels at $i_s^q = 66$ A.

tion where high power density per weight is required, e.g. as in drone propulsion drives. The initial design will be done using 2D finite element analysis (FEA) with focus on simple geometries to ensure manufacturability. As FEA software *COMSOL Multiphysics* is used. Two coil designs will be developed. One design consists of a classic full-material coil, while the second coil design will carry inserted cooling channels (CCs).

The electromagnetic design is mostly influenced by geometric limitations from the manufacturing process, compare Section 2.1. A summary of the initial 2D-design data is shown in Table 1. The length of the active iron part is set to $l_{Fe} = 9$ mm and the stator outer radius is $r_{s,o} = 66.5$ mm. While the application requires a high power density, the minimum mechanical clearance between adjacent parts of 0.5 mm is in contrast. In order to nevertheless achieve a high fill factor, the turns per coil will be set to $n_c = 5$. To make full use of the DC link voltage, a correspondingly high number of pole pairs $n_p = 11$ is selected.

Unlike the printed prototypes, in FEA simulations it is assumed that the stator and rotor are laminated (see Table 2). According to [31], CuCr1Zr with an electric conductivity of $\sigma_{el} = 43$ MS/m is used as coil material.

Starting from these initial constraints, a first design without cooling channels is made. The number of turns per coil combined with the minimum clearance and the chosen stator tooth dimensions leads to a wire cross section of $A_{Cu} = 7.7$ mm^2, which is kept constant across all coil layers. An overview of the resulting main machine data is listed in Table 3. Taking the defined current density into account, the rated current is $I_{s,R} = 47$ A$_{eff}$. Furthermore, because of the surface mounted permanent magnets, the inductance saliency ratio is $\lambda = L_s^q / L_s^d \approx 1$. Therefore, in the FEA only a q-axis current $i_s^q = 66$ A is used to produce the maximum torque. The absolute magnetic flux density at rated current for the 2D design is shown in Fig. 2. The resulting rated output power will be $p_{m,R} = 655$ W.

Besides the suitability of MM manufacturing, the possibility of providing the coil windings with inserted water cooling channels will also
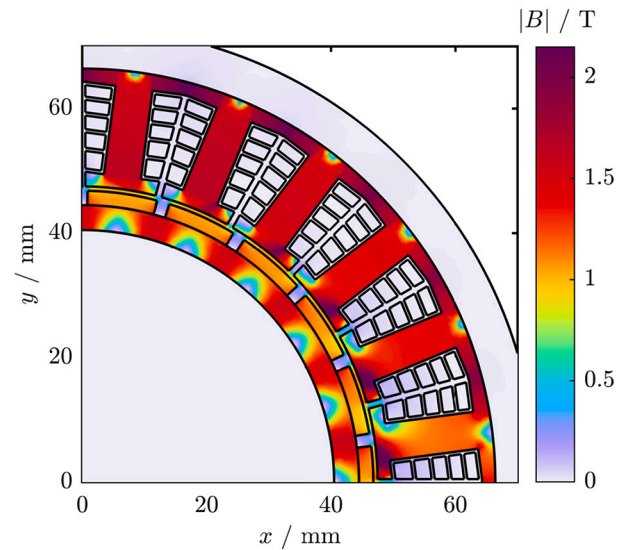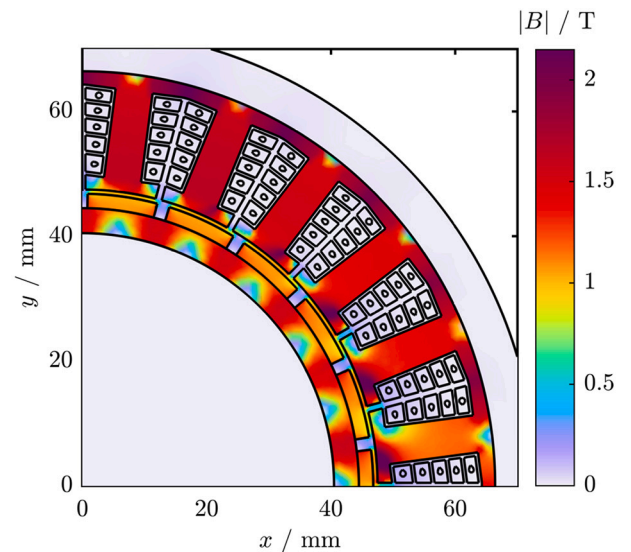
be investigated. The motivation of inserted cooling channels is to increase the heat dissipation, which leads to a lower winding temperature, decreases the copper losses and raises efficiency. Additionally, the rated current can be increased to reach identical temperatures as without cooling channels and therefore a higher power density is achieved.

The investigations are preliminary studies to establish printing feasibility. Hence, detailed simulations concerning the cooling performance of the channels are not performed for the time being. The cooling channel cross section is also kept constant across all coil layers to a value of $A_{CC} = 0.67$ mm^2. To ensure printability, the cross-section is designed so that the cooling channel resembles a teardrop shape. For this, the cross section of the channel must twist in the vertical area to ensure the right orientation of the teardrop shape in the area of a horizontal channel path. The finished design including cooling channels is shown in Fig. 3.

The rated motor speed of $n_m = 2000$ rpm in combination with $n_p = 11$ poles leads to a rated electric frequency of $f_p = 367$ Hz. Due to the skin and proximity effect, it is to be expected that current displacement occurs in the conductors, and thus increased copper losses compared to direct current (DC) will arise. The presence of cooling channels inside
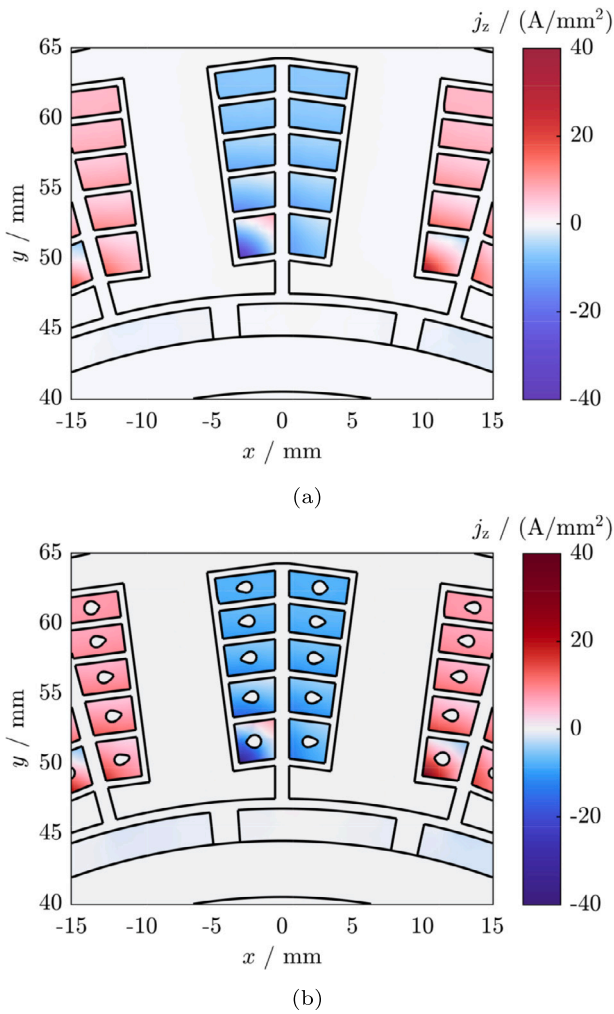
(a)

(b)

Fig. 4. Current density j_z in phase a at $n_m = 2000\,\mathrm{rpm}$ and $i_s^q = 66$ A; Without cooling channels (a); With cooling channels (b).

of the conductors will not only decrease the conducting area and therefore increase the DC losses, but also affect the alternating current (AC) resistance. To investigate the influence, both motors are simulated in FEA, excited by the rated current at different frequencies. Because of the 2D simulation, the end winding is neglected in this comparison.

The resistance ratio is calculated by

$$k_{\mathrm{Cu}} = \frac{P_{\mathrm{Cu,AC}}}{P_{\mathrm{Cu,DC}}}, \tag{1}$$

with

$$P_{\mathrm{Cu,AC}} = \frac{1}{T} \int_{t_0}^{t_0+T} \left(\frac{l_{\mathrm{Fe}}}{\sigma_{\mathrm{el}}} \sum_{i=1}^{n_{\mathrm{abc}}} \iint j_z^2(t) \mathrm{d}A_{\mathrm{Cu},i} \right) \mathrm{d}t, \tag{2}$$

where n_{abc} is the total number of turns per phase, j_z is the in-plane current density and T is the electric time period. The current density in both coils at rated speed is shown in Fig. 4.

Fig. 5 shows the results of the resistance ratio. As comparison, the AC resistance of both coil designs is normalized to the DC resistance of the coil design without cooling channel (WOCC). At low frequencies ($f_{\mathrm{el}} \to 0$ Hz), the DC resistance of the design with cooling channels is about 9% higher compared to the DC resistance without cooling channels, according to the 9% higher wire cross section without cooling channel. At a frequency of $f_{\mathrm{el}} = 1034$ Hz, both coil designs reach the identical coil resistance ratio of $R_{\mathrm{AC}}/R_{\mathrm{DC,WOCC}} = 3.42$, related to the DC value without cooling channels. At higher frequencies, the resistance

Table 4
Comparison of 2D and 3D FEA results.

Parameter	Symbol	2D	2D	3D	3D	Unit
CCs		No	Yes	No	Yes	
Copper area	A_{Cu}	7.8	7.1	7.8	7.1	mm²
Slot area	A_s	127.6	127.6	127.6	127.6	mm²
Filling factor	f_{fill}	60.9	55.6	60.9	55.6	%
Current density	$J_{s,R}$	6.0	6.6	6.0	6.6	A/mm²
DC resistance	R_{DC}			4535	5026	μΩ
Torque	m_M	3.13	3.13	2.76	2.76	N m
Rated power	$p_{\mathrm{m,R}}$	657	657	579	579	W
Power factor	$\cos(\phi)$	0.85	0.85	0.83	0.83	-

of the coil without a cooling channel exceeds that of the coil with a cooling channel.

2.3. Design adaption for PBF-LB/MM

Based on these requirements, the design of the coil is optimized for the PBF-LB manufacturing process. Minimum wall and gap dimensions as well as the maximum downskin angles have to be taken into account. The latter also causes the need for support structures whose removability after manufacturing must be ensured. Fig. 7a shows the design of the coils. To minimize the support structures between the core and the coil, the core and the coil converge at a 45° angle in the upper region. The support structures in the lower area can be removed after fabrication (Fig. 7c). The cooling channel has a drop-shaped cross-section, which twists depending on its position in the component (Fig. 7b). In addition, as shown in Fig. 7d, the radius of the channel is chosen to be as large as possible, both to reduce flow resistance during operation and to facilitate removal of the powder. The results of a initial manufacturing test of a part of the coil were analyzed in a micro-CT to ensure that the channel geometry can be manufactured. The CT-scans were made using a *Bruker SkyScan 1275*. The results are shown in Fig. 6. It can be seen that the droplet shape of the channels and its path was manufactured successfully.

A total of six coils were manufactured, three of them with a cooling channel. Fig. 8 shows the positioning in the pre-process within the Software *Autodesk Netfabb*, which is used to slice the designed part and to create the hatchlines for the filling of the parts.

2.4. 3D analysis of the adapted design

Finally, the design optimized for the printing process is examined in a 3D FEA simulation to test the effects of the special tooth and coil shape on the overall performance. Because no thermal simulations are done, only the design without cooling channels is simulated. The electrical conductivity of the stator and rotor core as well of the magnets was set to $\sigma_{\mathrm{el}} = 1$ S/m to avoid eddy currents. An example of the absolute magnetic flux density in the 3D model is shown in Fig. 9. To show the flux density in the iron core, some of the coils were hidden.

The comparison between the 2D FEA and the 3D FEA shows, that the mechanical output torque decreases about −12%. This is due to the deviation from a rectangular tooth shape, which leads to a reduced magnetic flux. Furthermore, it is assumed, that the presence of cooling channels in the 3D design will not affect the output torque, but only the copper losses. This effect can also be noticed in the 2D simulations. Finally, it is noticeable that the power factor decreases from $\cos(\phi)_{2D} = 0.85$ to $\cos(\phi)_{3D} = 0.83$. This can be explained by the increased magnetic leakage flux occurring at the winding head, which is taken into account in the 3D simulation.

3. Materials and methods

This section presents how the suitability of electric motor components for PBF-LB/MM fabrication were investigated.
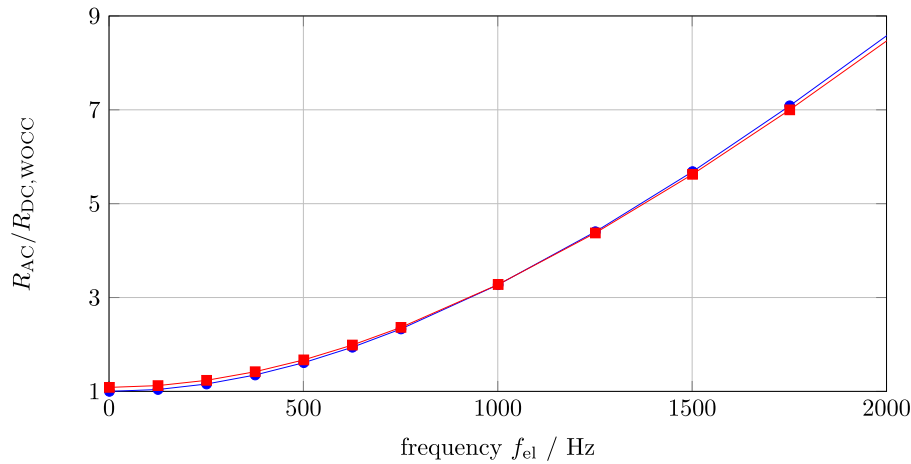
Fig. 5. AC resistance of the coils at rated current and different frequencies in relation to the DC resistance of the coil without cooling channel; without cooling channel [–], with cooling channel [–].
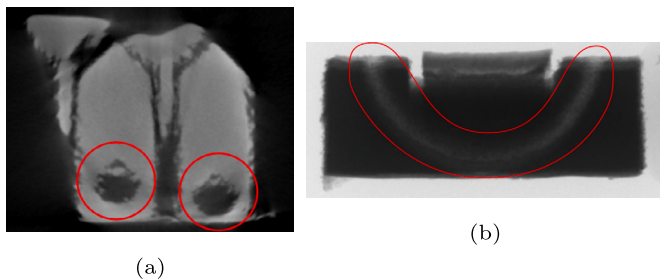

(a)

(b)

Fig. 6. CT-Scan of the cooling channels; cross section (a); channel path (b).

Table 6
Process parameters.

Parameter	Symbol	1.4404	CuCr1Zr	CuCr1Zr (remelting)	Unit
Layer thickness	s	40	40	40	μm
Wave length	λ_L	1070	1070	1070	nm
Laser power	P_L	150	400	400	W
Scanning velocity	v_{Scan}	600	600	650	mm
Hatch distance	h	0.08	0.12	0.12	mm
Focus diameter	d_s	0.08	0.08	0.08	mm

Table 5
Chemical composition of material feedstock.

CuCr1Zr feedstock						
Cu	Cr	Zr	Fe	Si		
bal.	1.05	0.12	0.02	< 0.004		

1.4404 feedstock						
Fe	**Cr**	**Ni**	**Mo**	**Mn**	**Si**	**others**
bal.	17.8	11.3	2.3	1.28	0.63	< 0.1

3.1. Material properties

The material used for the AM of the teeth is stainless steel 1.4404 and the copper alloy CuCr1Zr for the coils. 1.4404 was used as a core material despite its low soft-magnetic suitability, since the focus was on the feasibility study with regard to manufacturing. Since suitable manufacturing parameters are known for this material, 1.4404 is used [32]. The copper alloy CuCr1Zr has a low electrical conductivity in its initial state after the manufacturing process, but this can be increased by heat treatment. The chemical compositions of the material feedstocks used are shown in Table 5.

The coating principle of the MM powder deposition is based on rotating drums covered with a mesh. Therefore powder with a particle size distribution of 15 μm to 35 μm must be used. The exact particle size distribution of the 1.4404 and CuCr1Zr feedstock is shown in Fig. 10.

3.2. Manufacturing process

For the manufacturing of the coil in the PBF-LB/MM process, an *Aconity MIDI+* system is used, which is equipped with an *Aerosint* Recoater for the deposition of different powder materials. The Aconity MIDI+ system is a PBF-LB manufacturing system. It is equipped with a laser system, which includes two lasers with 1000 W and 500 W as well as a 3D scanning unit and a build platform that can be moved in the z-direction. Instead of a coater with brush or blade, however, a multimaterial recoater from *Aerosint* is installed, which can apply powder selectively on every layer. For this purpose, rotating drums are coated with a defined layer of powder by means of a vacuum, and this powder is ejected using individually controlled overpressure nozzles as it passes over the build platform. A multi-material powder bed can be generated by two of these coating drums [33]. The process parameters can be found in Table 6. Due to the poor absorption behavior of the copper alloy at a wavelength of $\lambda_L = 1070$ nm, a second exposure pass is performed (remelting).

3.3. Post processing

After the printing process, the coils are separated from the substrate plate, the support structure is removed and a heat treatment is applied to the coils and teeth to solidify the structure of the materials and mainly to increases the conductivity of the copper alloy.

The heat treatment process was carried out according to [34]. The coils are solution annealed at 980°C for 30 minutes in an argon inert gas atmosphere, followed by a cool-down phase at room temperature. In a second step, the coils are cured for three hours at 430°C, also in argon, and once again cooled down at room temperature.

After the heat treatment, a mechanical post processing is necessary to remove protruding metal residues and to ensure a sufficient distance between the coil layers. Also the last connection between the coil and the tooth has to be removed. Furthermore the winding must be isolated, on the one hand to avoid winding short circuits, and on the other hand to insulate the coil from the tooth. The isolation can be achieved by inserting isolation paper.
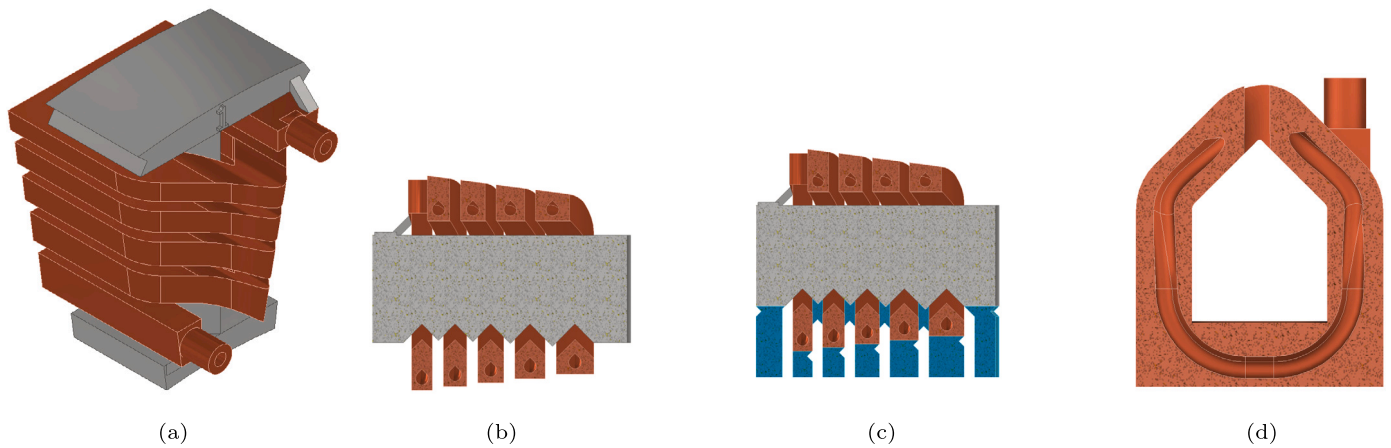
Fig. 7. Design of MM coils; final CAD-Design (a); cross section (b); support structure (c); path of the cooling channel (d).
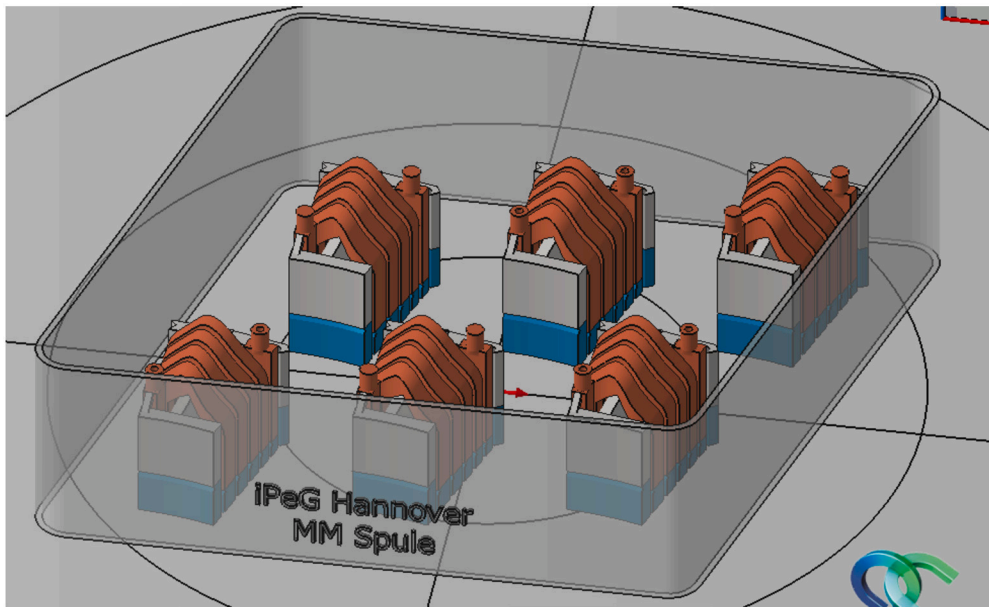

Fig. 8. Positioning of the coils on the substrate plate in Autodesk Netfabb. The frame ensures a level powder bed.
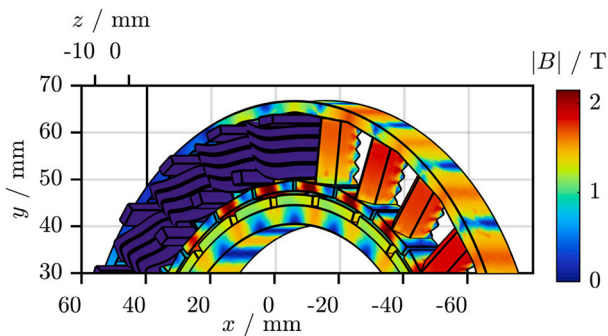

Fig. 9. Absolute magnetic flux density $|B|$ at $i_s^q = 66$ A.

3.4. Evaluation

The finished coils will be analysed regarding their geometric dimensional accuracy. Furthermore, the coils will be checked as for insulation and temperature dependent electric conductivity. Since the coil material is non-ferromagnetic, no magnetic tests are performed.

4. Results

In this section, the printed coils are further investigated with respect to their geometric shape and electrical properties. A total number of six coils was produced. Each coil has its own identification number, which is printed on the tooth. For consistency, the individual coils are described below with their numbers.

4.1. Manufacturing results

The six coils with a height of 22.6 mm were printed with 565 layers in a time of 38.5 hours. The process was constantly monitored in order to be able to intervene in the event of a process error and, if necessary, to refill the powder reservoir of the MM coater. In Fig. 11a, the process can be seen at a height of $z = 9.36$ mm. In addition to the 6 coils, the frame can also be seen, which prevents the powder bed from breaking off in the area of the components to be printed. After successful manufacturing, the substrate plate and the printed components are freed from unmelted powder, the components are separated from the substrate plate and the support structure is removed by mechanical post-processing. Unfortunately, the cooling channels could not be completely freed from unmelted powder. The printed result is shown in Fig. 11b.
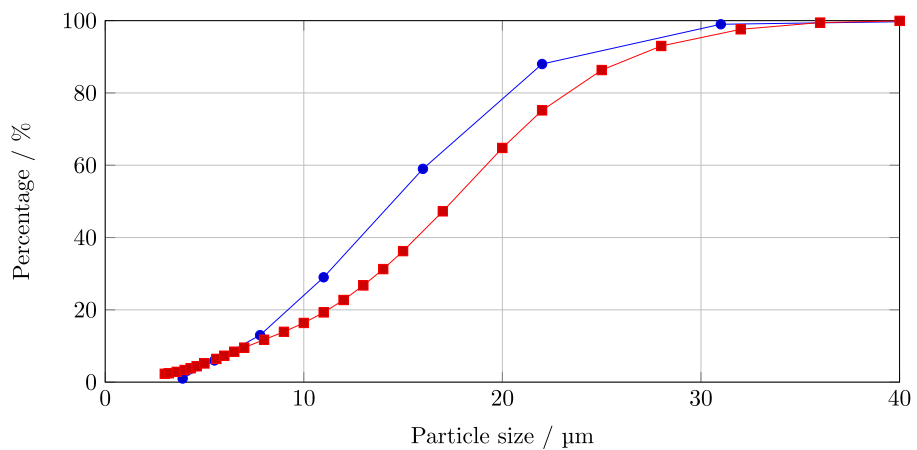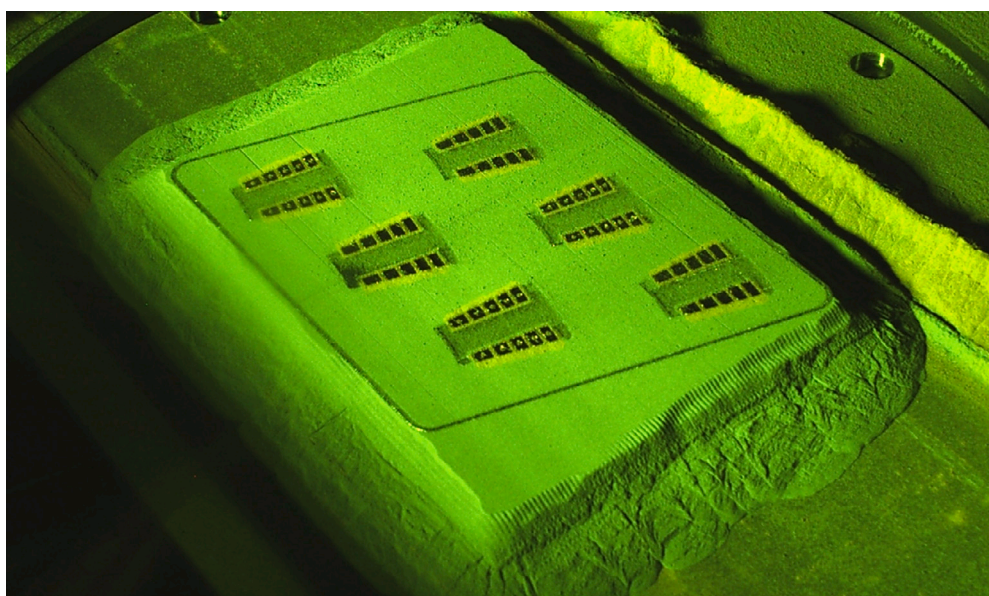
Fig. 10. Particle size distribution; 1.4404 [–], CuCr1Zr [–].

(a)

(b)

Fig. 11. PBF-LB/MM process and result; layer 234 at $z = 9.36$ mm (a); result on substrate plate (b).

All coils were visually inspected. The shape of the geometry deviations is the same for all coils, but the dimension of the deviation differs in some cases. A 3D scan was performed for the coil with the largest deformation. In order to compare the shape of the printed result with the nominal geometry, a 3D scan was performed with a *Zeiss COMET 5M* for the coil with most apparent geometric deviation. However, with this it is only possible to inspect the outer contour, while an inspection of narrow gaps or the inner channels is not possible, so that the 3D scan is only suitable for a qualitative representation of the distortion. Fig. 12 shows the deviation of the target geometry modeled in CAD from the actual geometry with the aid of a color scale. The strong deviation at the points of mechanical separation from the substrate plate and in the upper area of the coil winding is particularly clear. The former can be explained by inaccuracies in sawing off the support structures, since no clear reference surfaces are available. The reason for the latter is distortion due to thermal residual stresses. This is confirmed by the fact that this geometry deviation occurred only after cutting off from the substrate plate.

4.2. Heat treatment and isolation

From the printed six coils, four examples were picked for further investigations regarding electric material properties. In a first step, a heat treatment was done according to Section 3.3. Unfortunately, the argon atmosphere was not perfectly ensured. Therefore oxidation of the surfaces occurred and the face of the coils and teeth turned dark. The isolation between each coil layer was performed using the isolation paper *Nomex* 0.13 mm. Because of insufficient space between the copper turns and the teeth, it was not possible to insert isolation paper between
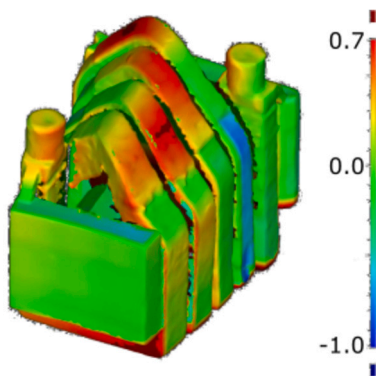

Fig. 12. Deviation of the actual geometry from the target geometry (in mm).

Fig. 13. Coil after the thermal treatment and adding isolation paper between the coil layers.

Table 7

Comparison of coil resistances after thermal treatment (ATT) to before thermal treatment (BTT) and FEA results.

Parameter Cooling channels	No. 3 No	No. 5 No	No. 2 Yes	No. 4 Yes	Unit
$R_{DC,FEA}$	567	567	628	628	μΩ
$R_{DC,BTT}$	1661	1695	1334	1951	μΩ
$R_{DC,ATT}$	731	615	540	746	μΩ
$\sigma_{ATT}/\sigma_{BTT}$	+127	+176	+147	+162	%
$\sigma_{ATT}/\sigma_{FEA}$	−22	−8	+16	−16	%
$R_{coil-tooth}$	35.9	35.8	3.2	36.2	mΩ

Table 8

Comparison of electric conductivity.

	Symbol	Cu IACS	CuCr1Zr [31]	CuCr1Zr $\overline{\sigma}_{ATT}$	Unit
Untreated	σ_{el}	58.0	20.0	14.3	MS/m
Treated	σ_{el}		43.0	36.4	MS/m

the coil and tooth. Fig. 13 shows the thermally treated and with isolation paper isolated coil. The brighter areas of the coil are indicate areas, where the surface was sanded after the thermal treatment.

4.3. Electric properties

The electric resistance was measured for each of the four coils before and after the thermal treatment, using a *Metrel MI 3242 Microohm 2A*. It should be noted that before thermal treatment, each coil was fixed to the core by a support structure to ensure the correct position of the coil. After the thermal treatment the support structure was removed. As shown in Table 7, the electric conductivity of each coil increased between +127% to +176% due to the thermal treatment. The coils No. 3, 5 and 4 have a higher DC resistance compared to the FEA results, while coil No. 2 has a lower resistance.

A continuity test between the teeth and coils has shown, that each coil was still in contact with the teeth. Therefore, the resistance between each coil and tooth was measured. While for the coils No. 3, 5 and 4 the contact resistance was about 50 times higher than their respective coil resistance, the contact resistance of coil No. 2 was only about 5 times higher than its coil resistance. Hence, it is expected that the coil No. 2 is affected by major short circuits, while the other three samples are not affected as much. As a result, coil No. 2 was not investigated further in the following tests. Furthermore, it is noticeable that the resistance without and with cooling channel hardly differs. This is due to the (still) present powder inside the cooling channels, which could not be removed, compare Fig. 6.

The measured coil resistance was used to calculate the mean electrical conductivity of the copper. The values from Table 4 are used for the average copper cross-section and coil length. The results are presented in Table 8. The mean of the values of the electrical conductivity after the thermal treatment is about 15% lower than the data sheet value [31], even though a parallel path cannot be excluded.

Furthermore, the temperature coefficient of the electrical resistance of the three coils No. 3, 5 and 4 was measured with a mean value of $\alpha = 0.00219\%/K$. The results are shown in Fig. 14.

5. Discussion

Within the scope of this article, it was shown that it is possible to manufacture coils consisting of different materials in a PBF-LB process. The potential offered by the degrees of freedom of AM with respect to electrical machines was identified. In particular, the possibility of integrating cooling channels can offer additional value to applications in which efficient high-performance drives are required. However, by
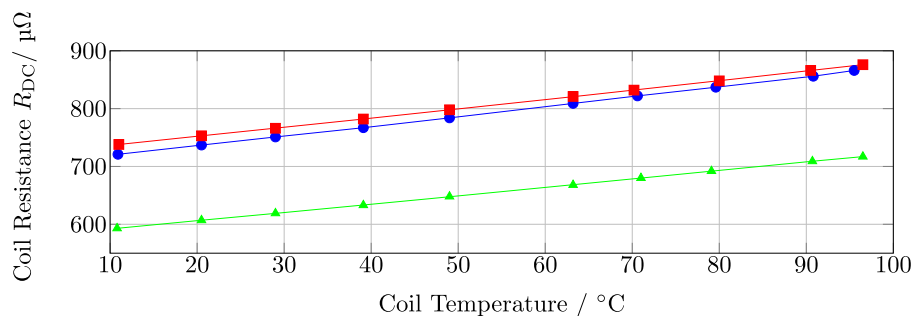
Fig. 14. Temperature dependent coil resistance; Without cooling channel: coil 3 [–] and coil 5 [–], with cooling channel: coil 4 [–].

manufacturing a multi-material component in one single process, limitations become clear. In terms of the manufacturing process, the available materials should be mentioned. The copper alloy CuCr1Zr is suitable as an electrical conductor due to the improvement of its material properties after heat treatment, which increased the electric conductivity of the copper alloy by +154%. In order to achieve a low remanence magnetic circuit, it is necessary to use a material with high magnetic permeability for the stator and rotor core. The stainless steel 1.4404, which is of low magnetic permeability, was mainly used because the process parameters for this material combination were already identified in previous work. In mono-material applications materials with high permeability were already additively manufactured [35]. Another limitation is the need for support structures in the PBF-LB process. To achieve subsequent isolation to avoid short-circuit currents, the component must be designed accordingly. As the results of the 3D FEA have shown, the corresponding adjustments in the studied example lead to a power reduction of −12%. To avoid support structures downskin angles must not be greater than 45°. If this is not possible, it must be ensured that the support structure is accessible for later separation. In addition, the work in this article has shown that, due to thermal distortion, the distance for the insulation of individual areas must be chosen larger than assumed. By performing the heat treatment before separation from the substrate plate, thermal distortion could also be reduced. Another way to guarantee the insulation between individual areas of the component is to use a different material or an additional material. By adding another coating drum with a non-conductive material, such as a ceramic material, an insulation can be ensured without the need for an air gap between certain elements of the entire component. The layers required for insulation could even be thinner than for insulation through an air gap, allowing for higher copper filling factors and thus higher efficiency due to a decreased thermal resistance. Although ceramic materials can also be processed with AM, the identification of suitable process parameters in combination with a copper alloy and a soft magnetic core material is challenging. Soft magnetic composites are an alternative, as they have good soft magnetic properties and are electrically non-conductive, which qualify them for being used as core material without an additional material for insulation.

6. Conclusion

Overall, it can be said that this article successfully investigated that it is possible to manufacture the tooth of an electric motor with concentrated winding consisting of two different materials using PBF-LB/MM. In addition to the electromagnetic design of the coil tooth, carried out by using 2D FEA, an optimization of the design with respect to the constraints imposed by the PBF-LB manufacturing process was also carried out. The influence of the mechanic adaptions on the output power was then examined using 3D FEA. Subsequently, it was shown that it is possible to produce MM components for electric drives with functional integration using the PBF-LB/MM process. Furthermore, an increase of the electrical conductivity of the copper alloy was achieved by heat treatment during post-processing. By measuring the electrical properties of the component as well as a 3D scan, it has been shown that the thermal distortion caused by the manufacturing process creates a strong geometry deviation, which ultimately also generates unwanted short-circuits between tooth and coil. In addition, it was not possible to remove the unmelted powder from the intended cooling channels. Based on these findings, solutions were presented by which an improvement in terms of coil functionality can be achieved. These include proposals for other or additional materials, in addition to adapting the geometric dimensions of the insulating air gaps and the cooling channels. Through these findings, the trade-off between complete insulation between different areas of the component and high efficiency through a high copper filling factor can be resolved.

CRediT authorship contribution statement

Marcus Oel: Conceptualization, Methodology, Investigation, Writing - Original Draft, Writing - Review & Editing, Visualization. **Johannes Rossmann**: Conceptualization, Methodology, Investigation, Writing - Original Draft, Writing - Review & Editing, Visualization. **Behrend Bode**: Conceptualization, Writing - Review & Editing. **Ina Meyer**: Investigation. **Tobias Ehlers**: Writing - Review & Editing. **Christoph M. Hackl**: Writing - Review & Editing, Resources, Supervision. **Roland Lachmayer**: Writing - Review & Editing, Resources

Declaration of competing interest

The authors declare that they have no known competing financial interests or personal relationships that could have appeared to influence the work reported in this paper.

Data availability

Data will be made available on request.

References

[1] A.S. Gohardani, G. Doulgeris, R. Singh, Challenges of future aircraft propulsion: a review of distributed propulsion technology and its potential application for the

all electric commercial aircraft, Prog. Aerosp. Sci. 47 (5) (2011) 369–391, https://doi.org/10.1016/j.paerosci.2010.09.001.

[2] B.A. Adu-Gyamfi, C. Good, Electric aviation: a review of concepts and enabling technologies, Transp. Eng. 9 (2022) 100134, https://doi.org/10.1016/j.treng.2022.100134.

[3] C.A. Luongo, P.J. Masson, T. Nam, D. Mavris, H.D. Kim, G.V. Brown, M. Waters, D. Hall, Next generation more-electric aircraft: a potential application for hts superconductors, IEEE Trans. Appl. Supercond. 19 (3) (2009) 1055–1068, https://doi.org/10.1109/TASC.2009.2019021.

[4] R. Lachmayer, T. Ehlers, R.B. Lippert, Entwicklungsmethodik für die Additive Fertigung, Springer Berlin Heidelberg, Berlin, Heidelberg, 2022.

[5] T. Ehlers, I. Meyer, M. Oel, B. Bode, P.C. Gembarski, R. Lachmayer, Effect-engineering by additive manufacturing, in: R. Lachmayer, B. Bode, S. Kaierle (Eds.), Innovative Product Development by Additive Manufacturing 2021, Springer International Publishing, Cham, 2023, pp. 1–19.

[6] R. Lachmayer, B.-A. Behrens, T. Ehlers, P. Müller, P. Althaus, M. Oel, E. Farahmand, P.C. Gembarski, H. Wester, S. Hübner, Process-integrated lubrication in sheet metal forming, J. Manuf. Mater. Process. 6 (5) (2022) 121, https://doi.org/10.3390/jmmp6050121.

[7] M. Binder, L. Kirchbichler, C. Seidel, C. Anstaett, G. Schlick, G. Reinhart, Design concepts for the integration of electronic components into metal laser-based powder bed fusion parts, Proc. CIRP 81 (2019) 992–997, https://doi.org/10.1016/j.procir.2019.03.240.

[8] T. Ehlers, S. Tatzko, J. Wallaschek, R. Lachmayer, Design of particle dampers for additive manufacturing, Addit. Manuf. 38 (2021) 101752, https://doi.org/10.1016/j.addma.2020.101752.

[9] F. Lorenz, J. Rudolph, R. Werner, Design of 3d printed high performance windings for switched reluctance machines, in: 2018 XIII International Conference on Electrical Machines (ICEM), IEEE, 2018, pp. 2451–2457.

[10] F. Lorenz, J. Rudolph, M. Weigelt, R. Werner, 3d printed high performance windings – prototypes and testing in a three phase srm, Electromechanical Drive Systems (2021), ETG Symposium 2021.

[11] C. Wohlers, P. Juris, S. Kabelac, B. Ponick, Design and direct liquid cooling of tooth-coil windings, Electr. Eng. 100 (4) (2018) 2299–2308, https://doi.org/10.1007/s00202-018-0704-x.

[12] J. Rudolph, N. Trnka, F. Lorenz, R. Werner, Vollstaendig 3d-gedruckte geschaltete reluktanzmaschine in klauenpolausfuehrung, E&I, Elektrotech. Inf.tech. 136 (2) (2019) 129–134, https://doi.org/10.1007/s00502-019-0707-y.

[13] C. Silbernagel, L. Gargalis, I. Ashcroft, R. Hague, M. Galea, P. Dickens, Electrical resistivity of pure copper processed by medium-powered laser powder bed fusion additive manufacturing for use in electromagnetic applications, Addit. Manuf. 29 (2019) 100831, https://doi.org/10.1016/j.addma.2019.100831.

[14] N. Simpson, D.J. North, S.M. Collins, P.H. Mellor, Additive manufacturing of shaped profile windings for minimal AC loss in electrical machines, IEEE Trans. Ind. Appl. 56 (3) (2020) 2510–2519, https://doi.org/10.1109/TIA.2020.2975763.

[15] F. Wu, A.M. EL-Refaie, A. Al-Qarni, Additively manufactured hollow conductors for high specific power electrical machines: aluminum vs copper, in: 2021 IEEE Energy Conversion Congress and Exposition (ECCE), 2021.

[16] H. Tiismus, A. Kallaste, A. Belahcen, A. Rassolkin, T. Vaimann, P.S. Ghahfarokhi, Additive manufacturing and performance of e-type transformer core, Energies 14 (11) (2021) 3278, https://doi.org/10.3390/en14113278.

[17] A. Mussatto, Research progress in multi-material laser-powder bed fusion additive manufacturing: a review of the state-of-the-art techniques for depositing multiple powders with spatial selectivity in a single layer, Results Eng. 16 (2022) 100769, https://doi.org/10.1016/j.rineng.2022.100769.

[18] M. Schneck, M. Horn, M. Schmitt, C. Seidel, G. Schlick, G. Reinhart, Review on additive hybrid- and multi-material-manufacturing of metals by powder bed fusion: state of technology and development potential, Progr. Addit. Manuf. 6 (4) (2021) 881–894, https://doi.org/10.1007/s40964-021-00205-2.

[19] S. Girnth, J. Koopmann, G. Klawitter, N. Waldt, T. Niendorf, 3d hybrid-material processing in selective laser melting: implementation of a selective coating system, Progr. Addit. Manuf. 4 (4) (2019) 399–409, https://doi.org/10.1007/s40964-019-00082-w.

[20] T. Stichel, T. Laumer, T. Baumüller, P. Amend, S. Roth, Powder layer preparation using vibration-controlled capillary steel nozzles for additive manufacturing, Phys. Proc. 56 (2014) 157–166, https://doi.org/10.1016/j.phpro.2014.08.158.

[21] X. Zhang, C. Wei, Y.-H. Chueh, L. Li, An integrated dual ultrasonic selective powder dispensing platform for three-dimensional printing of multiple material metal/glass objects in selective laser melting, J. Manuf. Sci. Eng. 141 (1) (2019), https://doi.org/10.1115/1.4041427.

[22] T. Bareth, M. Binder, P. Kindermann, V. Stapff, A. Rieser, C. Seidel, Implementation of a multi-material mechanism in a laser-based powder bed fusion (pbf-lb) machine, Proc. CIRP 107 (2022) 558–563, https://doi.org/10.1016/j.procir.2022.05.025.

[23] J. Walker, J.R. Middendorf, C.C. Lesko, J. Gockel, Multi-material laser powder bed fusion additive manufacturing in 3-dimensions, Manuf. Lett. 31 (2022) 74–77, https://doi.org/10.1016/j.mfglet.2021.07.011.

[24] C. Lesko, J. Walker, J. Middendorf, J. Gockel, Functionally graded titanium–tantalum in the horizontal direction using laser powder bed fusion additive manufacturing, JOM 73 (10) (2021) 2878–2884, https://doi.org/10.1007/s11837-021-04811-x.

[25] M. Hick, K. Eckes, C. Guillaume, A. Deblire, D.H.C.E. Moens, Device for Manipulating Particles, 2021.

[26] J. Foerster, M. Michatz, M. Binder, A. Frey, C. Seidel, G. Schlick, J. Schilp, Electrostatic powder attraction for the development of a novel recoating system for metal powder bed-based additive manufacturing, J. Electrost. 115 (2022) 103641, https://doi.org/10.1016/j.elstat.2021.103641.

[27] J. Foerster, K. Vranjes, M. Binder, G. Schlick, C. Seidel, J. Schilp, Electrophotographic powder application for metal powder bed based additive manufacturing, Proc. CIRP 113 (2022) 353–360, https://doi.org/10.1016/j.procir.2022.09.142.

[28] M. Bietags, Multi-material lpbf: 2x faster with machine learning, Online: https://www.x-t.ai/200-faster-multi-material-lpbf-with-machine-learning/, 2022. (Accessed 17 January 2023).

[29] M. Schneck, M. Horn, M. Schindler, C. Seidel, Capability of multi-material laser-based powder bed fusion—development and analysis of a prototype large bore engine component, Metals 12 (1) (2022) 44, https://doi.org/10.3390/met12010044.

[30] C. Singer, M. Schmitt, G. Schlick, J. Schilp, Multi-material additive manufacturing of thermocouples by laser-based powder bed fusion, Proc. CIRP 112 (2022) 346–351, https://doi.org/10.1016/j.procir.2022.09.007.

[31] Deutsches Kupferinstitut Berufsverband e.V., Datenblatt CuCr1Zr, Online: V. Deutsches Kupferinstitut Berufsverband e, Datenblatt CuCr1Zr, Online: https://kupfer.de/wp-content/uploads/2019/11/CuCr1Zr.pdf, 2022. (Accessed 29 November 2022).

[32] I. Meyer, M. Oel, T. Ehlers, R. Lachmayer, Additive manufacturing of multi-material parts – design guidelines for manufacturing of 316l/cucrzr in laser powder bed fusion, SSRN Electron. J. (2023), https://doi.org/10.2139/ssrn.4348515.

[33] I. Meyer, C.O. Messmann, M. Oel, T. Ehlers, R. Lachmayer, Multi-material pbf-lb/m process, https://doi.org/10.5446/62076.

[34] M. Habschied, S. Dietrich, D. Heussen, V. Schulze, Performance and properties of an additive manufactured coil for inductive heat treatment in the mhz range, HTM J. Heat Treatment Mater. 71 (5) (2016) 212–217, https://doi.org/10.3139/105.110294.

[35] D. Goll, D. Schuller, G. Martinek, T. Kunert, J. Schurr, C. Sinz, T. Schubert, T. Bernthaler, H. Riegel, G. Schneider, Additive manufacturing of soft magnetic materials and components, Addit. Manuf. 27 (2019) 428–439, https://doi.org/10.1016/j.addma.2019.02.021.